Front. Earth Sci. 2022, 16(3): 678–695
https://doi.org/10.1007/s11707-021-0941-6

RESEARCH ARTICLE

The capability of Sentinel-2 image and FieldSpec3 for detecting lithium-containing minerals in central Iran

Kazem RANGZAN (✉)[1], Mostafa KABOLIZADEH[1], Sajad ZAREIE[1], Adel SAKI[2], Danya KARIMI[1]

1 Department of Remote Sensing and GIS, Faculty of Earth Sciences, Shahid Chamran University of Ahvaz, Ahvaz 6135783151, Iran
2 Department of Geology, Faculty of Earth Sciences, Shahid Chamran University of Ahvaz, Ahvaz 6135783151, Iran

Abstract To date, there are very few studies about the spectroscopy of lithium-containing minerals (LCMs) in the scientific community. The main objective of this study is to investigate the capability of Sentinel-2 image and FieldSpec3 spectro-radiometer in terms of mapping five important LCMs, including spodumene, lepidolite, amblygonite, petalite, and eucryptite. Therefore, first the FieldSpec3 spectro-radiometer was used to create the spectral curves of the LCMs. Then, accurate spectral analysis and comparison of the studied LCMs were performed using The Spectral Geologist (TSG) and the Prism software. These two software can show even slight difference in absorption features of different LCMs, which can discriminate and identify these minerals. Lithium-bearing rocks show absorption features at ~365, ~2200, and ~2350 nm and reflective features at ~550–770 nm. These features are consistent with Sentinel-2 bands. Therefore, the created spectral curves were utilized for calibration of Sentinel-2 optical image to detect and map the potential zones of the rock units containing minerals mentioned above in a part of the central Iranian terrane. By using the Spectral Angle Mapper (SAM) classifier module, the potential areas were demarcated. Out of the five LCMs, petalite and spodumene showed more extensive coverage in the study area. Generally speaking, the largest concentration of those LCMs can be seen in southern and centraleastern parts of the study area. The comparison between spectral curves of reference and classified minerals confirmed the high capability of Sentinel-2 image for LCMs mapping. ASTER image classification results also confirmed the presence of the LCMs, but it cannot distinguish the LCMs type successfully.

Keywords FieldSpec3 spectro-radiometer, lithium containing minerals, Sentinel-2, ASTER, Iran

Received March 15, 2021; accepted August 10, 2021

E-mail: kazemrangzan@scu.ac.ir

1 Introduction

Due to the increasing demand for Lithium products, appropriate techniques of analyzing lithium (Li) chemical compounds, including lithium carbonate, lithium hydrate, lithium chloride, and lithium bromide, are required to search the rocks containing lithium in the Iranian geological terrane. The primary sources for lithium extraction are pegmatites and salars. Two of the most important producers of lithium are North America and Chile. North America mainly produces lithium carbonate from pegmatites, while Chile uses salars for lithium production. In the study of Alamdar et al. (2008), the presence of lithium-containing minerals (LCMs) in the pegmatites of the central Iranian terrane has been confirmed using field survey and spectrographic analyzes. Some research has been conducted on the study of lithium minerals using remote sensing (Rossi et al., 2018; Cardoso-Fernandes et al., 2019a, 2019b, 2020, 2021; Gao et al., 2020). Cardoso-Fernandes et al. (2019b) applied Landsat-5, Landsat-8, Sentinel-2, and ASTER images for identifying Li-pegmatites through alteration mapping and the direct identification of Li-bearing minerals. They utilized new RGB (red, green, blue) combinations, band ratios, and selective principal component analysis (PCA) as processing methods. For example, RGB 1613, 2113, and 5114 of ASTER image were applied for identifying Li-pegmatites, and 1/3, 6/2, and 12/9 ASTER band ratios were implemented for spodumene, lepidolite, and amblygonite identification. Their results showed excellent potential for the identification of Li-bearing pegmatites using remote sensing. Also, they concluded that their results could be improved using sensors with a better spatial and spectral resolution. Gao et al. (2020) applied a combination of geochemical methods, geological mapping, and high-resolution remote sensing multispectral imagery to identify potential locations of pegmatite-hosted Li occurrences. In their study, reflectance spectra were obtained from spodumene-bearing pegmatite samples on the ground surface using the FieldSpec-3 spectrometer. They

found that the spodumene-bearing pegmatites show a strong absorption at ~2200 and ~2350 nm, and reflective features between 560 and 760 nm. Because of the limited data available for the whole study area, they used the combined Worldview-2 and ASTER remote sensing images. Their results proved successful in discovering several significant Li deposits.

According to the results of the study of about lithium isotopes, lithium absorption features occur in the visible range of electromagnetic radiation. Travis and Kendall (2017) applied thermal infrared spectroscopy for lithium quantification within greisen-style mineralogy. Their study showed that absorption near 1411 and 2200 cm^{-1} shifted to higher wavelengths in samples with the highest lithium. Based on the results of previously mentioned works, it can be concluded that lithium has absorption features in the electromagnetic radiation range of VNIR (Visible and Near-Infrared), SWIR (Short Wave- Infrared), and TIR (Thermal-Infrared). However, based on our knowledge, there is no record on the spectroscopy of different LCMs (at NNIR-SWIR wavelengths) for studying their spectral curves simultaneously so far.

Spectroscopy describes the interaction between electromagnetic radiation and materials, which produces a spectral curve of material in a specific wavelength range (Clark, 1999; Cloutis et al., 2010). The chemical composition of any mineral determines its nature of interaction with the electromagnetic radiation that may cause several physical processes such as absorption, reflection, transmission, and scattering, which contain important information about the mineral types. A unique reflectance spectral curve is produced for every mineral due to its response to electromagnetic radiation. Using these spectral curves and spectral characteristics, one can identify the minerals. The absorption of electromagnetic energy at wavelengths is the result of several processes, including electronic and vibrational. Absorption characteristics of minerals in VNIR result from an electronic process that is due to the presence of Ni, Cr, Co, Fe, Mn, Li, etc., elements in the combination of minerals (Zaini, 2009; Kruse, 2010). The vibrational processes of hydroxyl ion (OH^-), the water molecule (H_2O), carbonate, etc., define the absorption characteristics of minerals in the SWIR range (Zaini, 2009). An absorption range of the hydroxyl ion is around 1400 nm, while absorption characteristic of the minerals containing hydroxyl ion and water molecule occurs around 1900 nm wavelength. The interaction between hydroxyl and metal ions (e.g., Al and Mg) that produce hydroxyl combinations (e.g., AlOH and MgOH) causes a vital absorption characteristic in the range of 2200–2300 nm (Zaini, 2009). Spectroscopy has many applications (Tappert et al., 2013; Afsharifar and Rangzan, 2014; Zheng et al., 2016; Cao et al., 2017; Guha et al., 2018). Zheng et al. (2016) reviewed the changes over time of five pedogenic soil properties of a chronosequence, i.e., soil organic matter, iron oxide, clay minerals, particle size distribution, and calcium carbonate using reflectance spectroscopy. Guha et al. (2018) used the spectroscopy and ASTER data processing to detect dolomite-hosted phosphate around Udaipur city in western India. The results showed that their method could be useful to detect Phosphate zones in similar geological settings. The results of their study conducted by Cloutis et al. (2010) demonstrated that spectra with a resolution of 0.34 nm could show the most robust spectral reflection of ortho-pyroxenes and clinopyroxenes at 506 nm wavelength. They concluded that their results could be considered a powerful tool to determine the combination and structure of pyroxenes. Zaini (2009) identified the occurrence of strong vibrational absorption using the spectroscopy at 2.34 and 2.5365 μm for pure calcite and ranges of 2.32138 and 2.51485 μm for pure dolomite.

The main objective of this study is to investigate the capabilities of Sentinel-2 image and FieldSpec3 for LCMs mapping in a part of central Iran. Another objective of the present study is to compare the spectral characteristics of five important LCMs accurately. The presence of LCMs in the central Iranian terrane has been confirmed by Alamdar et al. (2008), for which the study area was chosen. In the first step, the reflectance and absorption characteristics of the LCMs available in the mineralogical museum of the Department of Geology at the Shahid Chamran University of Ahvaz were created using FieldSpec3. Furthermore, using TSG and Prism software, the spectral curves were analyzed. Then, based on spectra of the LCMs and using the SAM classifier and Sentinel-2 image, a part of the central Iranian terrane was mapped to show the potential zones. Finally, LCMs classification was also done using ASTER image and the results were compared.

2 Study area and geological setting

The chosen study area is a part of the central Iranian terrane located between 34°17'38" and 33°18'48" northern latitudes and 53°44'24" and 54°55'55" eastern longitudes (Fig. 1).

2.1 The central Iranian terrane

The right part of Fig. 1 shows the litho-structural map of Iran, showing the main Iranian geological zones (Berberian and King, 1981). The central Iranian terrane is one of the most critical and intricate structural zones in Iran that is located in the center of the Iran litho-structural map. This area is bordered by the Alborz Mountains in the north, the Lut Block in the east, and the Sanandaj–Sirjan in the south-south-west (Stocklin, 1968). Several stages of metamorphism, magmatism, and orogeny are related to orogenic events, and the age of the rocks is from Precambrian to Quaternary (Ghorbani, 2016). This

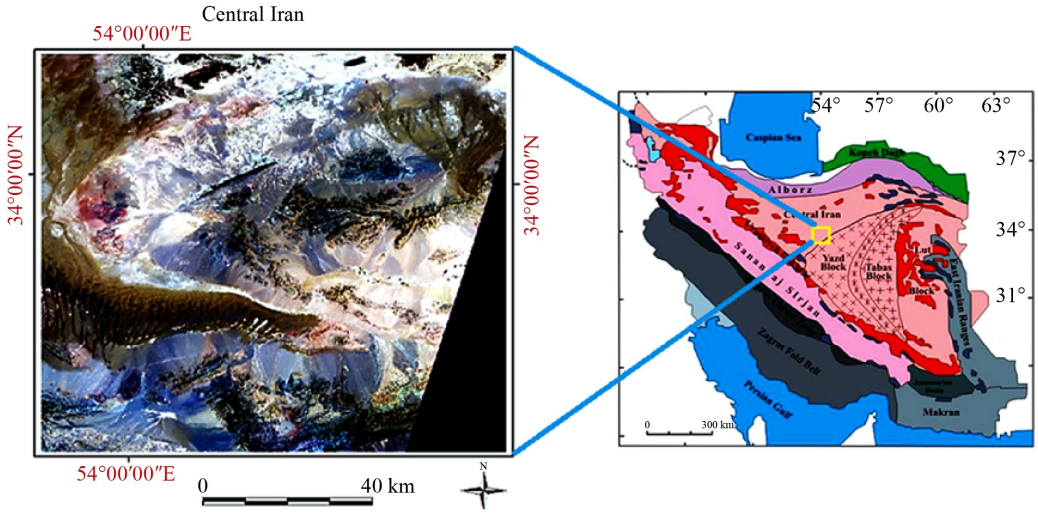

Fig. 1 Location of the study area and geological setting.

terrane formed in pre-Paleozoic shows no indication of any Variscan overprint (Delaloye et al., 1981). Magmatism occurred in the central Iranian terrane from Precambrian to Cenozoic. Precambrian Igneous rocks are not abundant in this area. However, Late Neoproterozoic arc-related magmatism (Rahmati, 2010), the extensive basaltic eruption in Silurian (Derakhshi et al., 2014), and Devonian Anarak basic magmatism are some of them. Metamorphic rocks cropped out in some regions of the central Iranian terrane, including DehSalm, Anarak, Khar Turan, and Saghand. The metamorphic rocks are mainly composed of the alteration of schist, phyllite, amphibolite, and marble layers with Paleozoic to Cenozoic ages (Rahmati, 2010). During the Mesozoic, several large intrusive bodies appeared in the central Iranian terrane, namely Shirkuh, Shahkuh, and Troudgranitoid. This fact is due to the subduction process of the Neo-Tethys oceanic crust under the Iran microplate (during the Alpine orogenesis) (Soltani, 2000; Shah et al., 2014). Magmatic activity in the Cenozoic was affected by volcanism that is known as the Urumieh-Dokhatr magmatic assemblage. This event caused volcanic rocks and some igneous bodies having acidic combinations (Amidi and Michel, 1985).

2.2 Central Iranian terrane pegmatites

The results of mineralogical studies and chemical analyses of the central Iranian terrane pegmatites (based on) are presented in Table 1.

3 Material and methods

3.1 FieldSpec3 spectro-radiometer

FieldSpec3 spectro-radiometer manufactured by Analytical Spectral Devices, Inc., Boulder, Colorado, the USA with good efficiency in the laboratory, can measure the reflection, transmission, and radiation of different materials. This instrument is an optical device with a spectral range of 350–2400 nm that has a collection time of 0.1 s for each spectrum. FieldSpec3 works in three ranges of electromagnetic wavelengths including 350–1000 nm (VNIR), 1000–1830 nm (SWIR1), and 1830–2400 nm (SWIR2) (Rangzan et al., 2019; Afsharifar and Rangzan, 2014).

3.2 The TSG and Prism software

Using substantial similarity matching algorithms, TSG software (available at CSIRO website) can quickly and accurately investigate a similarity of the studied minerals with the minerals found in its library and finally present the similarity matching results, because of having a rich library of minerals. The current TSG library consists of 60 classes which are 1) Mica group (illite, muscovite, phengite, and paragonite); 2) other AlOH minerals (montmorillonite, prehnite, pyrophyllite, topaz); 3) kaoline (well-crystallized kaolinite, poorly crystallized kaolinite, dickite, andnacrite); 4) amphiboles (tremolite, actinolite, hornblende, and riebeckite); 5) three varieties of chlorite (magnesium, iron, and intermediate); 6) sulphates (jarosite, gypsum, and three varieties of alunite); 7) a variety of other MgOH and FeOH bearing minerals (biotite, phlogopite, nontronite, talc); 8) carbonates (calcite, dolomite, ankerite, magnesite, and siderite); 9) epidote and opaline silica (Rangzan et al., 2020).

The Prism can be used as an add-on tool for ENVI software to analyze the spectra using the United States Geological Survey (USGS) spectral library (available at USGS website). This library is a widely used library containing thousands of spectra of the minerals, vegetation, and manufactured materials (Clark, 1999). Prism can quickly and accurately calculate spectral specifications like absorption range, area of the absorption, depth of the absorption feature, full width at half maximum (FWHM) of the absorption feature, etc.

Table 1 Spectrographic analysis results of the central Iranian terrane pegmatites (Alamdar et al., 2008)

Sampling site	Sample No.	Elements/10^{-6}					Lithium-containing minerals
		Ba	Li	Be	Ga	Nb	
Yazd Shirkuh	1	60	40	<3	10	-	amblygonite, spodumene, lepidolite
	2	45	60	<3	12	<30	
	3	250	50	7	14	-	
Robat-e-Posht-e-Badam	4	45	60	4	11	-	amblygonite, petalite, lepidolite
	5	55	40	5	40	11	
	6	250	120	12	100	11	
Chadormaloo	7	60	40	<3	18	-	amblygonite, spodumene, lepidolite
	8	400	60	4	30	<15	
	9	180	40	6	11	-	
Eastern Jandag	10	45	120	<13	12	-	amblygonite, spodumene, lepidolite, petalite
	11	40	120	13	35	-	
	12	35	80	9	10	<30	

3.3 Continuum removal

Continuum removal normalizes the studied spectra, and therefore the values will be set between 0 and 1. The continuum is a convex hull fitted to a curve between two of its end points. The continuum can be described as follow (Liu and Han, 2017):

$$x_l(i) = k(i - I_l) + x(I_l), \tag{1}$$

where $x(i)$ is a spectral band to be normalized, and k is the slope of a continuum. k is calculated by the following formula:

$$k = \frac{x(I_r) - x(I_l)}{I_r - I_l}, \tag{2}$$

where I_l and I_r are the indices of the end points. Therefore, continuum-removal is as follow:

$$C_r[x(i)] = \frac{x(i)}{x_l(i)}. \tag{3}$$

3.4 The studied LCMs

The LCMs studied in this research are spodumene, amblygonite, petalite, lepidolite, and eucryptite provided by the mineralogy museum of the Department of Geology of the Shahid Chamran University of Ahvaz (Fig. 2). Table 2 shows the characteristics of the LCMs mentioned above (Meshram et al., 2014). The following table shows the theoretical amount of lithium in the minerals described above studied by other workers in few countries.

The spectral curves of the studied LCMs obtained using the FieldSpec3 spectro-radiometer from a distance of about 2 cm. The radiance spectrum was normalized to that of a standard white reference panel (99% standard). To reduce the noise level, the FieldSpec3 was kept stationary and ~100 spectra were recorded. As mentioned before, based on the study of Birch et al. (1978), a spectral behavior of the lithium isotopes indicated that the lithium element absorption usually occurs in the visible range of electromagnetic radiation, especially in the purple, blue, green, and red bands. Also, based on Gao et al. (2020), Li-bearing samples show absorption features at ~2200 nm, and ~2350 nm and reflective features at ~550–770 nm. These features are consistent with Sentinel-2 bands. Therefore, the spectral features will be searched at the VNIR-SWIR wavelength of the obtained spectral curves. Then, absorption area, FWHM (full width of the absorption at the half depth of it), absorption depth (measured in a continuum removed curve from a convex hull to the deepest point of the absorption feature), absorption center (the exact wavelength in the middle of the absorption feature), absorption range (e.g., 2200–2300 nm) of the absorption features on the spectral curves will be measured using PRISM software and will be compared. Those are spectral absorption parameters which are very important for separating spectral curves.

3.5 Satellite images

Sentinel-2 optical satellite was launched in the year 2015, with a 7-year operational period to land monitoring, including vegetation, water, soil, and coasts, preparation of land use and change detection maps, land cover studies, water change monitoring, and climate changes. The height of this sun-synchronous satellite is 786 km, the angle of the orbit is 98.5 degrees, and it has a repeat cycle of ten days, which is five days due to the simultaneous existence of two satellites. The Sentinel-2 satellite image contains 13 bands of optical range and 10–60 m spatial resolution. These images are geometrically and radiometrically corrected that can be downloaded for free from the European Space Agency or ESA (available at ESA website). The utilized Sentinel-2 image (S2A platform) date in the present study is July

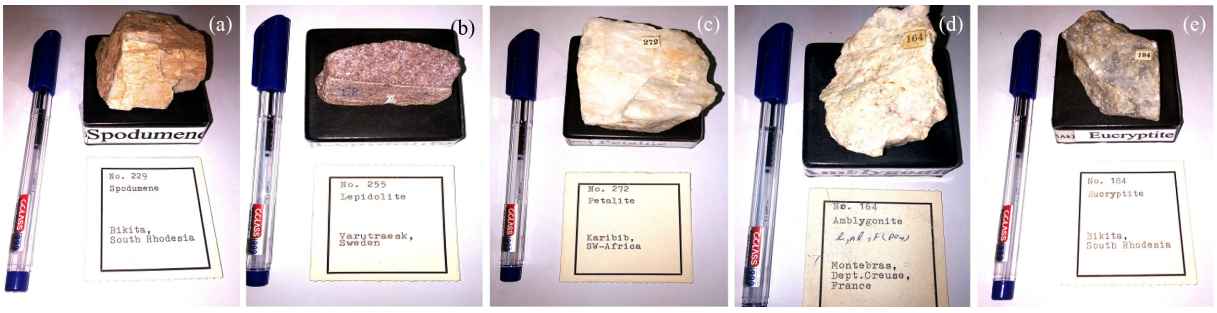

Fig. 2 The studied LCMs available in the mineralogical museum of the Department of Geology: (a) spodumene, (b) lepidolite, (c) petalite, (d) amblygonite, and (e) eucryptite.

Table 2 LCMs characteristics (Meshram et al., 2014) and their formula

Lithium-containing minerals	Theoretical amount of Li% (w/w)		Formula	Maximum concentration in the world
	Range	Center		
Spodumene	3.3–1.9	2.6	$LiAlSi_2O_6$	Australia
Lepidolite	3.6–1.53	2.565	$KLiAl_{1.5}(F,OH,O_{0.5})_2(AlSi_3O_{10})$	Zimbabwe
Amblygonite	4.2–3.5	3.85	$LiAlPO_4(F,OH)$	Canada, Brazil, Surinam
Petalite	2.1–1.6	1.85	$LiAlSi_4O_{10}$	Zimbabwe
Eucryptite	–	2.34	$LiAlSiO_4$	Zimbabwe

2018. Atmospheric correction of the image was performed using the Sen2Cor module and therefore the reflectance values were obtained. The spectral curve of each image pixel will be compared to the LCMs spectral curves using the SAM classifier in terms of mapping the LCMs in the study area. The atmospheric correction will produce reflectance values in the range of 0–1. The FieldSpec3 spectral curves are also in the range of 0–1. Sentinel-2 bands are in the range of 443–2190 nm which is almost the same as the FieldSpec3. Therefore, the SAM classifier can classify the study area accurately without the need for more image preprocessing. The results of this classifier based on the error percentage will be displayed as follow: Percent error = [(Exact value–Approximate value)/Exact value] × 100.

The ASTER multispectral data was acquired in September 2003. The image was geometrically corrected and only atmospheric correction was applied and therefore reflectance values were obtained. The spectral bands of the ASTER image contain NIR and SWIR bands with a resolution of 15 m. Three bands of the ASTER between 520 and 860 nm (VNIR B1-B3) and six bands from 1600 to 2430 nm (SWIR B4-B9) are for measuring reflectance radiations. Also, five bands in the 8120–11650 nm wavelength region (TIR B10–B11) with 90 m spatial resolution are for measuring emitted radiation (Gao et al., 2020). Table 3 shows the specifications of the image.

3.6 The Spectral Angle Mapper (SAM) classification method

The SAM measures and assesses the similarities of the spectra using the following equation (Kuching, 2007):

$$a = \cos^{-1}\left(\frac{\sum_{i=1}^{nb} t_i r_i}{\sqrt{\sum_{i=1}^{nb} t_i^2}\sqrt{\sum_{i=1}^{nb} r_i^2}}\right), \quad (4)$$

where nb is the number of image bands, t is the pixel spectrum, r is the reference spectrum, and a is the spectral angle. Less amount of a shows more similarity of the image spectrum with the reference spectrum and vice versa.

3.7 The Spectral Information Divergence (SID) classification method

The Spectral Information Divergence (SID) is a spectral classification method that uses a divergence measure to match pixels to reference spectra. The smaller the divergence, the more similar the pixels are. Pixels with a measurement more than the specified maximum divergence threshold are not classified. Reference spectra used by SID can come from spectral libraries (Du et al., 2004).

4 Results

In this study, the LCMs absorption characteristics in the VNIR and SWIR ranges were recorded by the FieldSpec3 spectro-radiometer. All processing steps were performed in the spectrometry laboratory of remote sensing and GIS department of the Shahid Chamran University of Ahvaz, without destruction of the samples. However, due to the

small size of mineral samples, the contact probe device that is one of the main tools of the FieldSpec3 was used to improve the accuracy of the spectra with less or no atmospheric noises. This device can measure 2×2 cm^2 area of the samples. Then, the spectral curves of the LCMs were studied and compared using the TSG software. A continuum removal, absorption center, absorption depth, FWHM, and other characteristics were determined using the Prism software. The spectral and absorption characteristics of five important LCMs, including spodumene, lepidolite, amblygonite, petalite, and eucryptite, were assessed, and finally, the classification was implemented. The following sections will be discussed the above-mentioned steps carefully.

As mentioned in Section 3.5, the utilized Sentinel-2 image was geometrically and radiometrically corrected, which is downloaded for free from the ESA website. The utilized Sentinel-2 image (S2A platform) date in the present study is July 14, 2018. Atmospheric correction of the image was performed using the Sen2Cor module. Therefore, its values convert to reflectance values (Section 3.5).

4.1 Assessing the LCMs using the TSG

As previously mentioned, having a rich library of the minerals and substantial similarity matching algorithms, the TSG can quickly and accurately investigate the similarity of the minerals. Finally, the TSG presents the similarity matching results as a percentage. Figure 3 shows the stacked reflectance curves extracted by using the TSG for all the five LCMs.

The continuum removal described in Section 3.3 was applied for a more accurate comparison of the LCMs. The same procedure was used in the Prism to find the absorption characteristics. In addition, this method can remove the effects of the grain size and topography (Noda and Yamaguchi, 2017). Figure 4 shows the stacked spectra of the continuum removed LCMs using the TSG, and Fig. 5

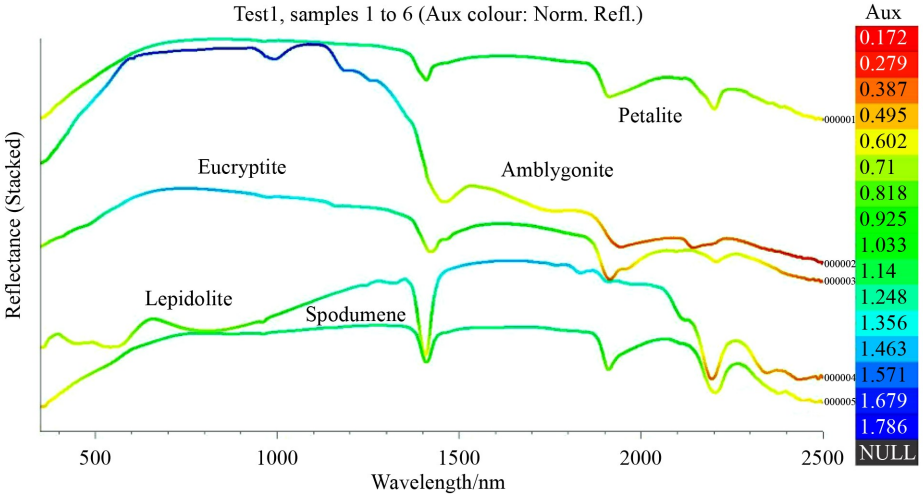

Fig. 3 The stacked spectra of LCMs using the TSG software.

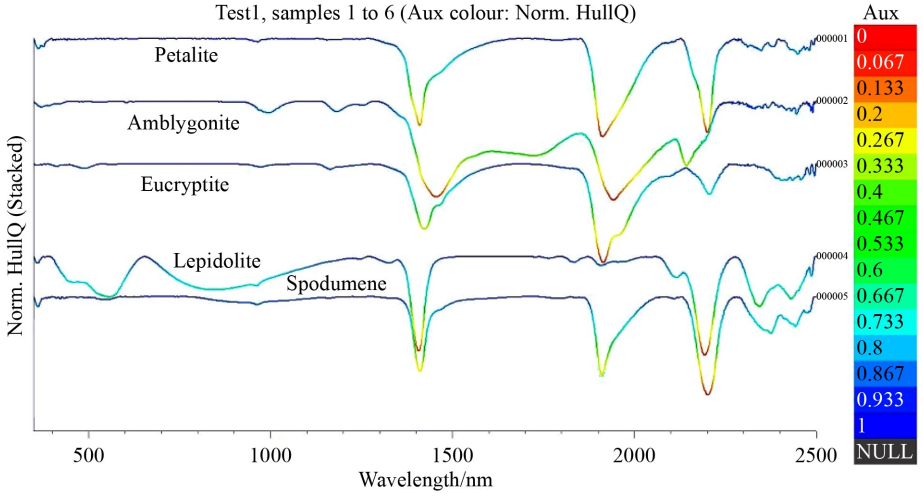

Fig. 4 The stacked spectra of the continuum removed LCM using the TSG software.

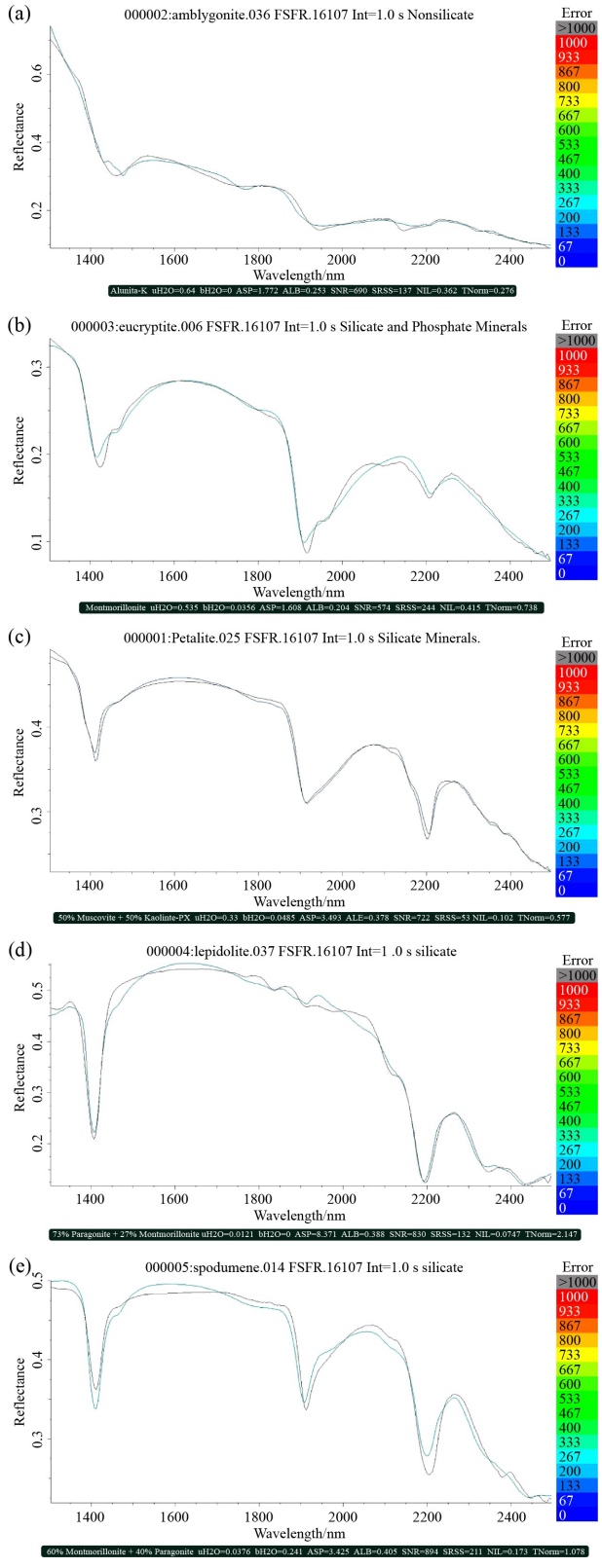

Fig. 5 Spectral similarity matching of (a) amblygonite, (b) eucryptite, (c) petalite, (d) lepidolite, (e) spodumene using the TSG software.

shows the similarity matching process of the TSG.

A summary of the specific features of the identified minerals similar to the LCMs was obtained using the TSG (Fig. 6).

4.1.1 Analyzing and identifying Lithium element absorption based on the TSG

As mentioned before, the study of the spectral behavior of the Lithium isotopes by Birch et al. (1978) indicated that the Lithium element absorption usually occurs in the visible range of the electromagnetic radiation, especially purple, blue, green, and red bands. The most considerable absorption of this element in the LCM is observed from purple to blue bands (Fig. 7).

4.2 Analyzing and identifying Lithium element absorption based on the Prism software

In this step, the absorption characteristics of the Li element in spodumene, lepidolite, amblygonite, petalite, and eucryptite, were assessed using the Prism software and the obtained results were compared (Fig. 8). The absorption characteristics of the Li element, OH^{-}, H_2O, and hydroxyl combination in the studied LCMs are shown in Table 4.

4.3 Sentinel-2 data output

In the processing step, the SAM classifier was applied and the output data was obtained as Fig. 9, the results of which will be interpreted in Section 5.3.

5 Discussion

5.1 The TSG outputs

The TSG software is a specialized spectral analysis tool designed specifically for the mining and exploration industry geoscientists. In this study, the TSG has been used to analyze the studied LCMs. The TSG outputs are displayed in Figs. 4–8.

One of the most essential analytical processes performed by the TSG is similarity matching between the input studied minerals and its robust spectral library, as described in Section 3.2. The results of this step indicate the minerals that have specific characteristics near the given wavelength (e.g., SWIR wavelength range of 1400–2500 nm, in which the TSG will perform an accurate similarity matching). Based on the results presented in Fig. 5, the mineral having specific characteristics similar to amblygonite is alunite-k (Fig. 5(a)), and the mineral containing specific characteristics similar to eucryptite is montmorillonite (Fig. 5(b)). 50% of the specific characteristics of petalite are similar to muscovite, and another 50% is similar to Kaolinite (Fig. 5(c)).

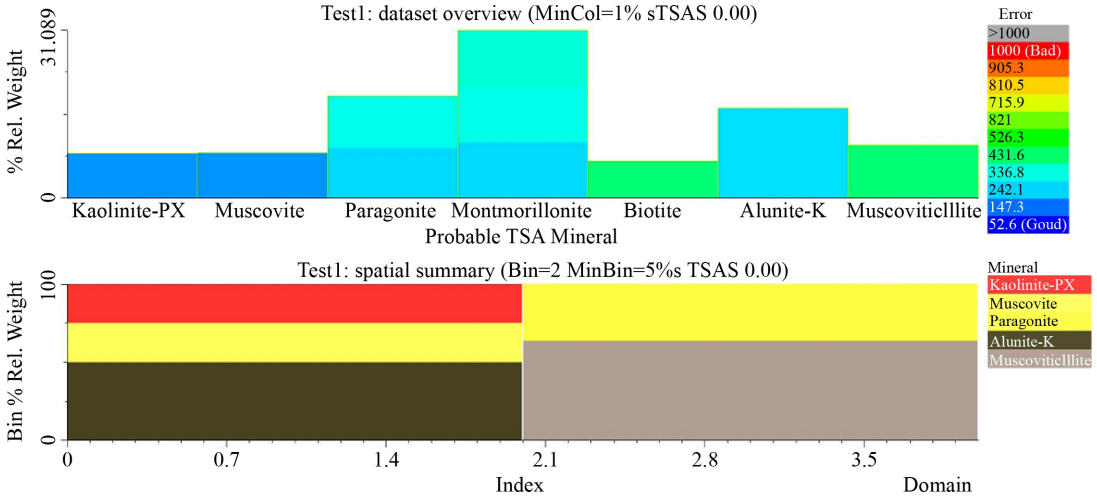

Fig. 6 Analyzing the identified minerals in the lithium samples using the TSG.

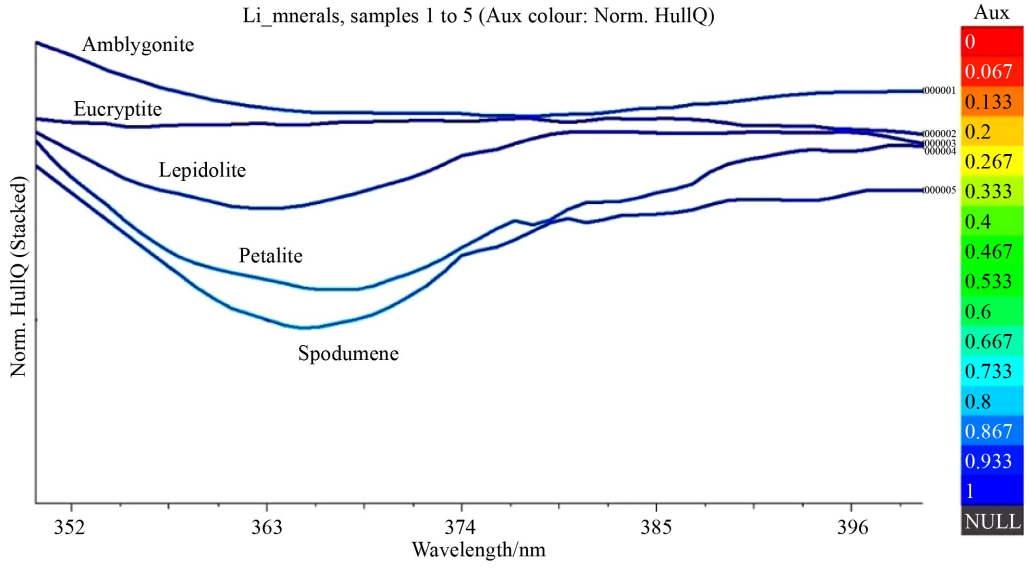

Fig. 7 Lithium absorption range indifferent LCM using the TSG.

Lepidolite has 73% of the specific characteristics similar to paragonite, and 27% similar to montmorillonite (Fig. 5(d)), and finally, spodumene contains 60% of the specific characteristics similar to montmorillonite and another 40% similar to paragonite (Fig. 5(e)). These percentages are obtained as a report below each figure of the TSG similarity matching outputs by the software (Fig. 5).

5.2 The Prism outputs

The exact characteristics, including the center of the absorption range, FWHM, the absorption area, slope, and ratio of the continuum, were calculated for the determined absorption ranges using the Prism. Some of the resulted data by calculating the absorption characteristics are summarized in Table 3. Using the Prism outputs, the absorption ranges of the minerals can be easily compared, and their differences can be detected.

The most crucial absorption feature of the LCMs is the lithium element absorption (Fig. 8). Based on Fig. 10 and Table 3, even slight differences in the lithium absorption feature can be seen in the studied LCMs. For example, the lithium absorption center in spodumene, lepidolite, amblygonite, eucryptite, and petalite was 362, 357, 370, 360, and 372 nm, respectively, which can be used as a factor for LCMs discrimination. There is a direct and positive correlation between the absorption depth of an element and its amount in a mineral. As can be seen in Table 3, the absorption depth of the lithium in amblygonite, spodumene, eucryptite, lepidolite, and petalite is 13.7, 20.5, 1.1, 46.1, and 13.6, respectively. Therefore, it may be concluded that lepidolite contains more amount lithium, and eucryptite has the least amount of lithium in comparison to the other LCMs. Other spectral characteristics such as the absorption center of OH^- show shift in spodumene, lepidolite, amblygonite, eucryptite, and petalite at 1410 nm, 1408 nm, 1451 nm, 1423 nm, and 1410 nm, respectively (Fig. 10). In

Table 3 Specifications of the used satellite images

#	Satellite images	Wavelength/nm	# Bands	Spatial resolution/m
1	Sentinel-2	443–2190	13	10–60
2	ASTER	520–2430	14	15–90

Table 4 The results obtained by analyzing the absorption characteristics of LCM using the Prism software

Lithium-containing minerals	Absorbers	Absorption area /(μm×ref)	FWHM/nm	Absorption depth	Absorption center/nm	Absorption range/nm
Spodumene	lithium	0.0002861	12.7	0.0205	362	352–377
	OH^-	0.009	34.3	0.2423	1410	1355–1458
	H_2O	0.019	60.3	0.2731	1913	1865–2050
	Hydroxyl combination	0.021	58.5	0.3477	2202	2132–2262
Lepidolite	lithium	0.0004908	10.4	0.0461	357	352–371
	OH^-	0.024	38.9	0.5758	1408	1350–1455
	H_2O	0.0013	30.8	0.0392	1906	1869–1935
	Hydroxyl combination	0.032	52.2	0.5864	2194	2137–2250
Amblygonite	lithium	0.0002383	16.7	0.0137	370	353–388
	OH^-	0.041776	105	0.3849	1451	1300–1530
	H_2O	0.04776	121.7	0.3858	1946	1860–2090
	Hydroxyl combination	0.01384	77.2	0.2043	2145	2100–2237
Eucryptite	lithium	0.0000021	2	0.0011	360	352–362
	OH^-	0.04043	88.2	0.4038	1423	1350–1600
	H_2O	0.05815	97	0.6099	1915	1840–2040
	Hydroxyl combination	0.00967	46.2	0.1860	2208	2140–2255
Petalite	lithium	0.0003154	25.1	0.0136	372	355–391
	OH^-	0.00750	40	0.1758	1410	1348–1450
	H_2O	0.02586	101.3	0.2536	1915	1855–2056
	Hydroxyl combination	-	41.6	0.2427	2202	2120–2245

addition, the FWHM of OH^- in spodumene, lepidolite, amblygonite, eucryptite, and petalite is 34.3 nm, 38.9 nm, 105 nm, 88.2 nm, and 40 nm, respectively.

The H_2O absorption center also exhibits a shift in different LCMs. As it can be seen in Table 3, the H_2O absorptioncenter in spodumene, lepidolite, amblygonite, eucryptite, and petalite is 1913 nm, 1906 nm, 1946 nm, 1915 nm, and 1915 nm, respectively (Fig. 11).

5.3 The SAM classification using Sentinel-2 image

As mentioned before, a Sentinel-2 (S2A) optical image of July 14, 2018 containing 13 bands and spatial resolution of 10 m×10 m was used to determine the potential places of LCMs in part of the central Iranian terrane. Therefore, the study area was classified using the Spectral Angle Mapper (SAM). A geometrically corrected S2A image was downloaded from the ESA and then atmospheric correction of the image was performed using the Sen2Cor module.

The spectral curves of the studied LCMs were used as end-members for the SAM. An automated SAM method is used for comparing image spectra with individual spectra or with a spectral library (Kruse, 2010). The results of the SAM classifier are displayed in Fig. 12. SAM classifier has been implemented using ENVI 4.8 software, and its outputs have been displayed on Google Earth.

Placemarks in part *a* are some of the locations of potential LCMs in part of the central Iranian terrane, and Figs. 12(b)–12(e) are the zoom-in parts of part *a*, which display different LCMs in the study area. As shown in Fig. 12, the amount of petalite and spodumene is the highest in the study area. In addition, other LCMs such as eucryptite and amblygonite were also observed in several places in the study area. The main concentration of the LCMs was observed in the southern and central-eastern parts of the study area. As previously mentioned, the presence of the LCMs of spodumene, amblygonite, petalite, and lepidolite in the pegmatite rocks of the central Iranian terrane was confirmed using field survey and spectrographic analysis by Alamdar et al. (2008). According to the spectrographic analyses of the pegmatitic rocks of the central Iranian terrane by Alamdar

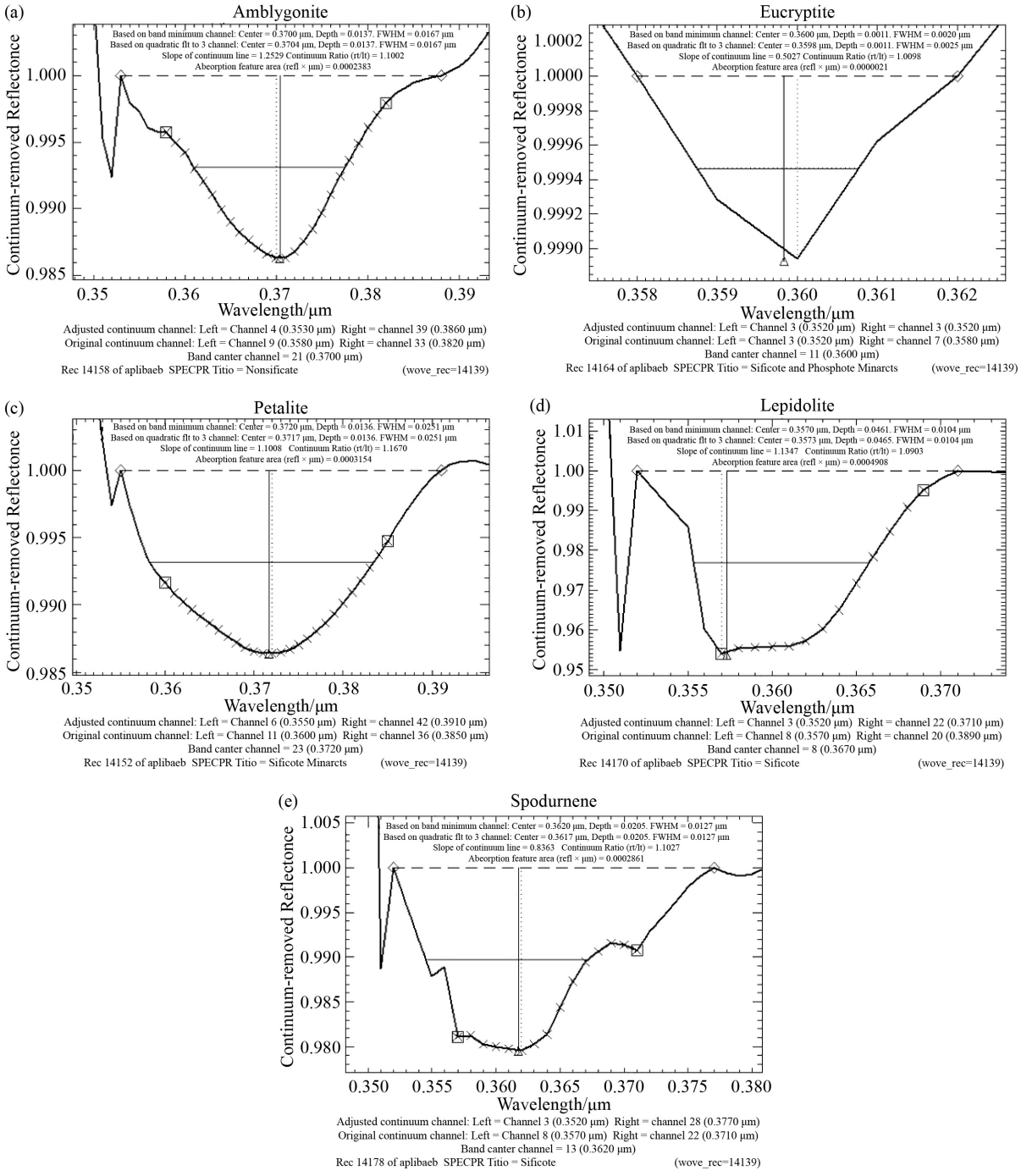

Fig. 8 Analyzing and identifying Li element absorption in (a) amblygonite, (b) eucryptite, (c) petalite, (d) lepidolite, and (e) spodumene using the Prism software (all the numbers mentioned in (a)–(e) are summarized in Table 3).

et al. (2008), their Lithium amount was between 40×10^{-6} and 60×10^{-6} in Yazd Shirkuh, 40×10^{-6}–120×10^{-6} in Robat-e-Posht-e-Badam, 40×10^{-6}–60×10^{-6} in Chador-maloo, and 80×10^{-6}–120×10^{-6} in the east of Jandag. It should be noted that sampling performed by Alamdar et al. (2008) was limited and discrete. While classification results obtained in the present study are continues and cover a wide area. Since Alamdar et al. (2008) sampling of the study area was carried out as points, some of the results may be incomplete (e.g., unlike SAM results, Alamdar et al. (2008) did not sample and recognize eucryptite mineral in the study area). As mentioned before, eucryptite has been recognized in several places (green color in Fig. 12) in the study area (e.g., 33°26'37.78"N latitude and 54°27'5.06"E longitude). It should be noted that the samples provided by the mineralogy museum of the Department of Geology of the Shahid Chamran University of Ahvaz were considered as reference spectrum in this study, and the research of Alamdar et al. (2008) was considered as field survey and

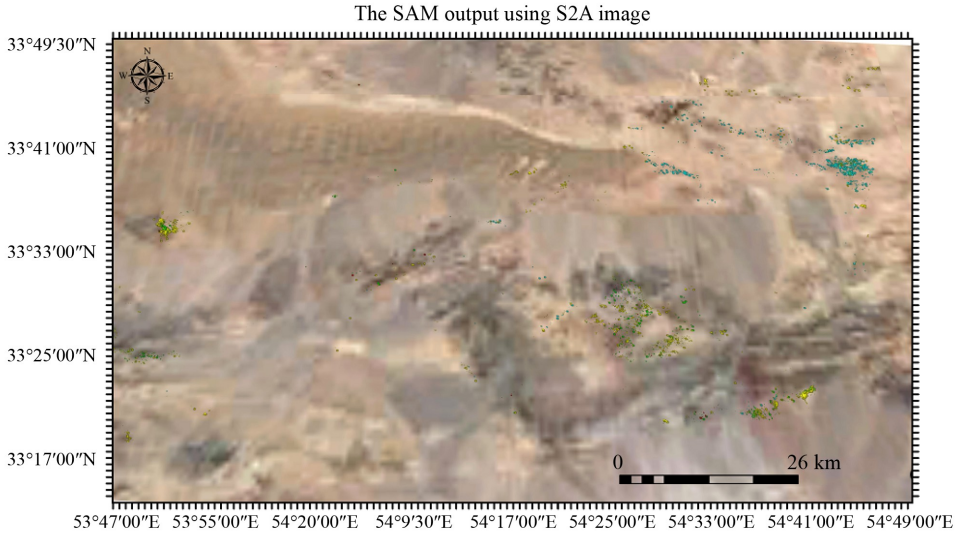

Fig. 9 The SAM output using S2A image.

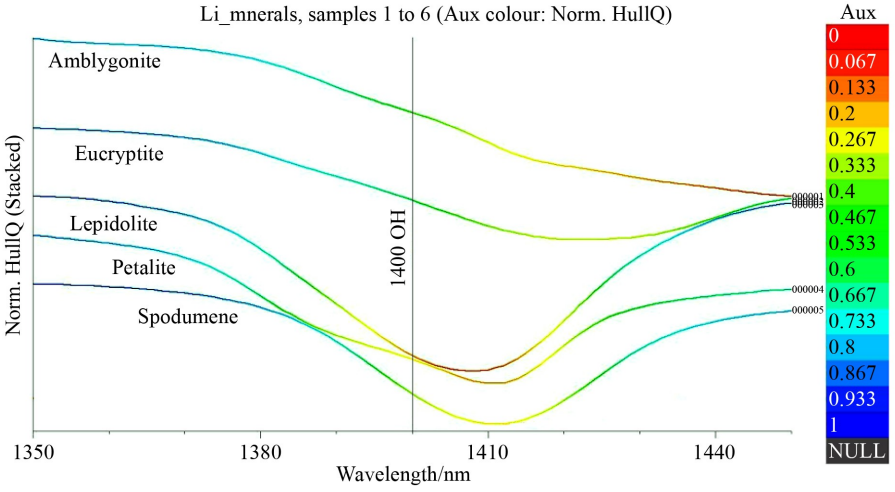

Fig. 10 The absorption center of OH^- in the LCMs.

spectrographic analysis. Therefore, ground photos of the minerals are not available. In the following, a detailed comparison of the spectral curves of the recognized minerals obtained from the classification and the reference minerals will be performed to validate the results. Also, quantitative results validation will be done in Section 5.4 (Table 5).

It can be concluded that the SAM is an appropriate classification method, due to providing accurate results for spectrum similarity of the input samples and ground samples by using an accurate examination. The satellite image of Sentinel-2, due to having 13 bands in the VNIR and SWIR wavelengths, is very appropriate data for various studies such as geological studies. The spectroscopy method and the SAM classification of the Sentinel-2 image indicated the high capability to map the rare minerals such as the LCMs. It should be noted that based on the objective of this research which is assessing the capability of Sentinel-2 image and FieldSpec3 spectro-radiometer for LCM mapping, this image was chosen. As mentioned before the specific reflectance and absorption features of LCMs (absorption feature at ~2200, and ~2350 nm and reflective features at ~550–770 nm based on Gao et al. (2020)) are consistent with Sentinel-2 bands. Also, compared to other free optical images, the Sentinel-2 is a new satellite with good spatial, spectral, and radiometric resolutions and because of the ability of free download.

To validate the results of the SAM classification (qualitative accuracy assessment), the spectral curves of the extracted LCMs using the SAM classifier have been compared to the spectral curves of the studied reference LCMs (Fig. 13). Based on the ENVI statistical analysis, SAM identified all five LCM. However, an exact position of lepidolite could not be found to compare spectral curves. Therefore, another SAM classification has been performed to map only lepidolite mineral. The result shows that the SAM classifier could not recognize any

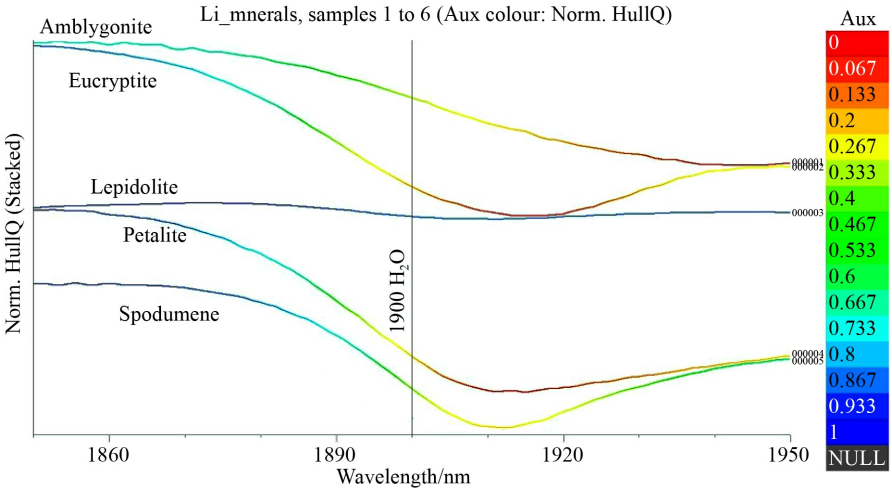

Fig. 11 The absorption center of H_2O in LCM.

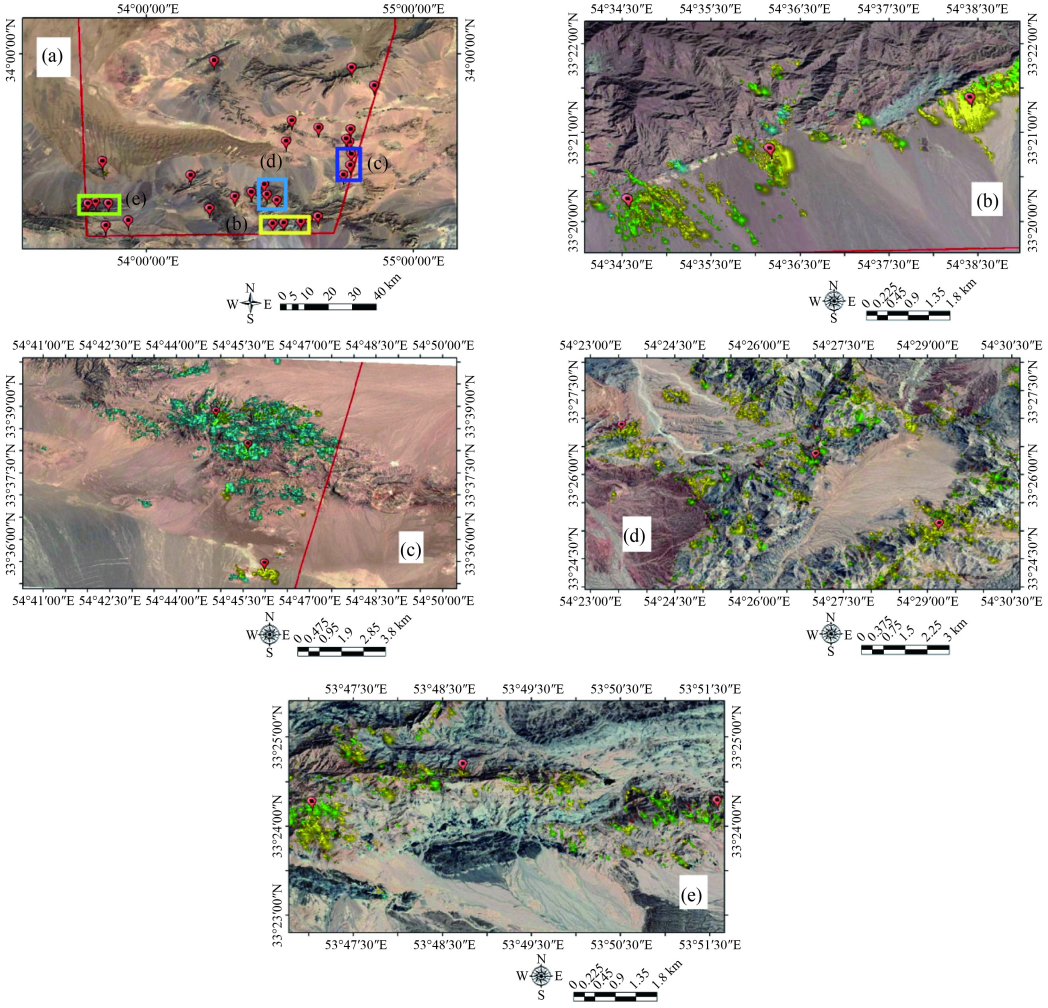

Fig. 12 The outputs of the SAM classification method displayed on Google Earth: (a) some of the locations of LCMs (b)–(e).

lepidolite in the study area. Considering that, the SAM classification method compares the spectrum of one pixel of a Sentinel-2 image (with a spatial resolution of 10 m × 10 m) with each of the reference spectra, the lack of a classification of this mineral in the study area indicates its low spatial distribution. In other words, the distribution is less than the pixel size of the image. Therefore, according to the proof of the existence of this mineral in the region by Alamdar et al. (2008) to classify it, an image with a smaller pixel size, another classification method or

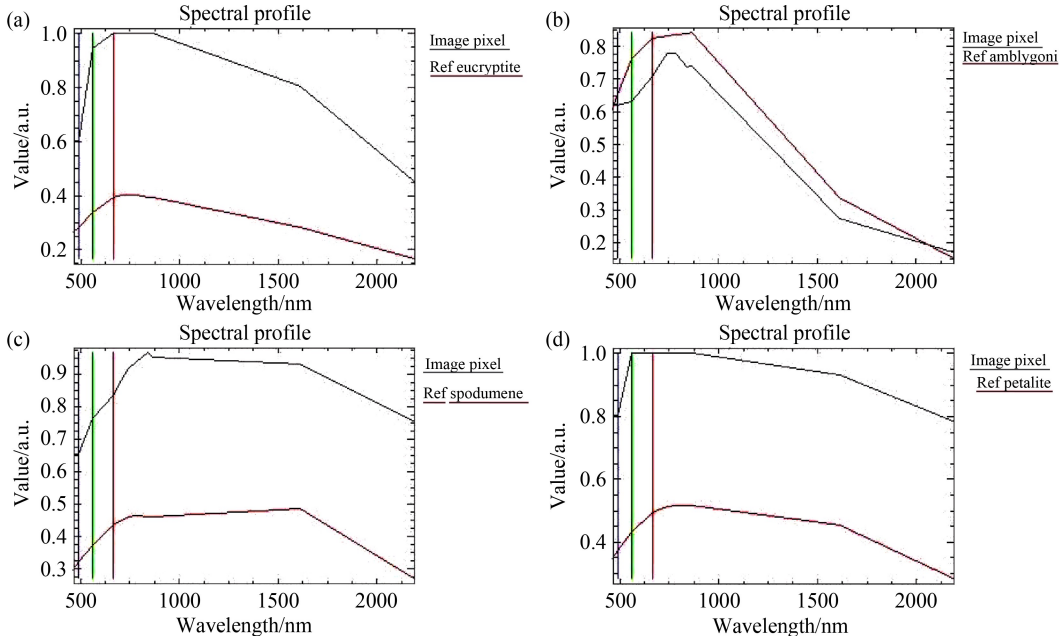

Fig. 13 The similarity matching of (a) eucryptite, (b) amblygonite, (c) spodumene, and (d) petalite.

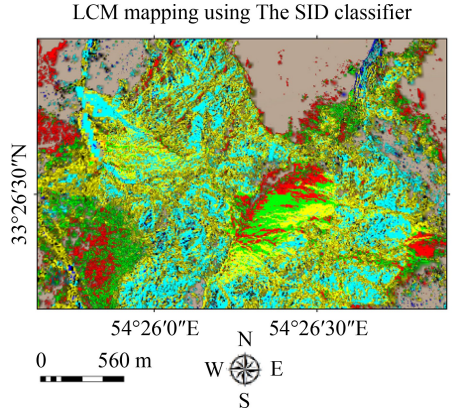

Fig. 14 LCM mapping using the SID classifier and Sentinel-2 image.

applying image like ASTER which is suitable for geological studies should be tested. Thus, Sections 5.4 and 5.5 will discuss applying the SID classifier and the ASTER image for LCM mapping.

Based on the results shown in Fig. 13, the spectral curves of the SAM results in the present study are well matched to the reference studied LCMs. Therefore, it can be concluded that the results of the SAM classification are reliable and have high accuracy.

5.4 The SID classification using Sentinel-2 image

In terms of a better validation of the results, the SID classification method was also implemented (Fig. 14), and its results were compared to the SAM results. Figure 15 displays similarity matching of the extracted LCM spectral curves based on the SID classifier and the studied reference LCMs.

Table 5 Accuracy assessment of the SAM and SID results (%)

	Eucryptitie	Ambligonite	Spodumene	Petalite	Lepidolite
SAM	80	70	90	90	–
SID	20	50	10	20	20

In terms of quantitative validation and comparison of the SAM and the SID results, ten classified pixels of each class were chosen. The spectral curves of the chosen pixels were compared to the reference LCM spectral curves, and therefore, the error has been calculated based on the number of unmatched spectra (Table 5).

As can be seen in Table 5, the SAM classifier obtained the best results while the SID results are poor.

5.5 LCM mapping using ASTER image

In terms of improving the spatial resolution of the ASTER image, image fusion of the ASTER image and band 2 of the Sentinel-2 image has been implemented based on the Gram-Schmidt fusion method (Pohl and Van Genderen, 2016). Therefore, the output ASTER image has a 10 m spatial resolution. As mentioned before, ASTER 2113, 5114, and 1613 RGBs are useful for LCMs mapping (Cardoso-Fernandes et al., 2019a, 2019b). Therefore, in this step, the above-mentioned RGBs were applied for LCM mapping using ASTER image. The following figure shows lithium regions identified by the above RGBs compared to the SAM results using the S2A image.

As shown in Fig. 16, unlike the SAM results, ASTER

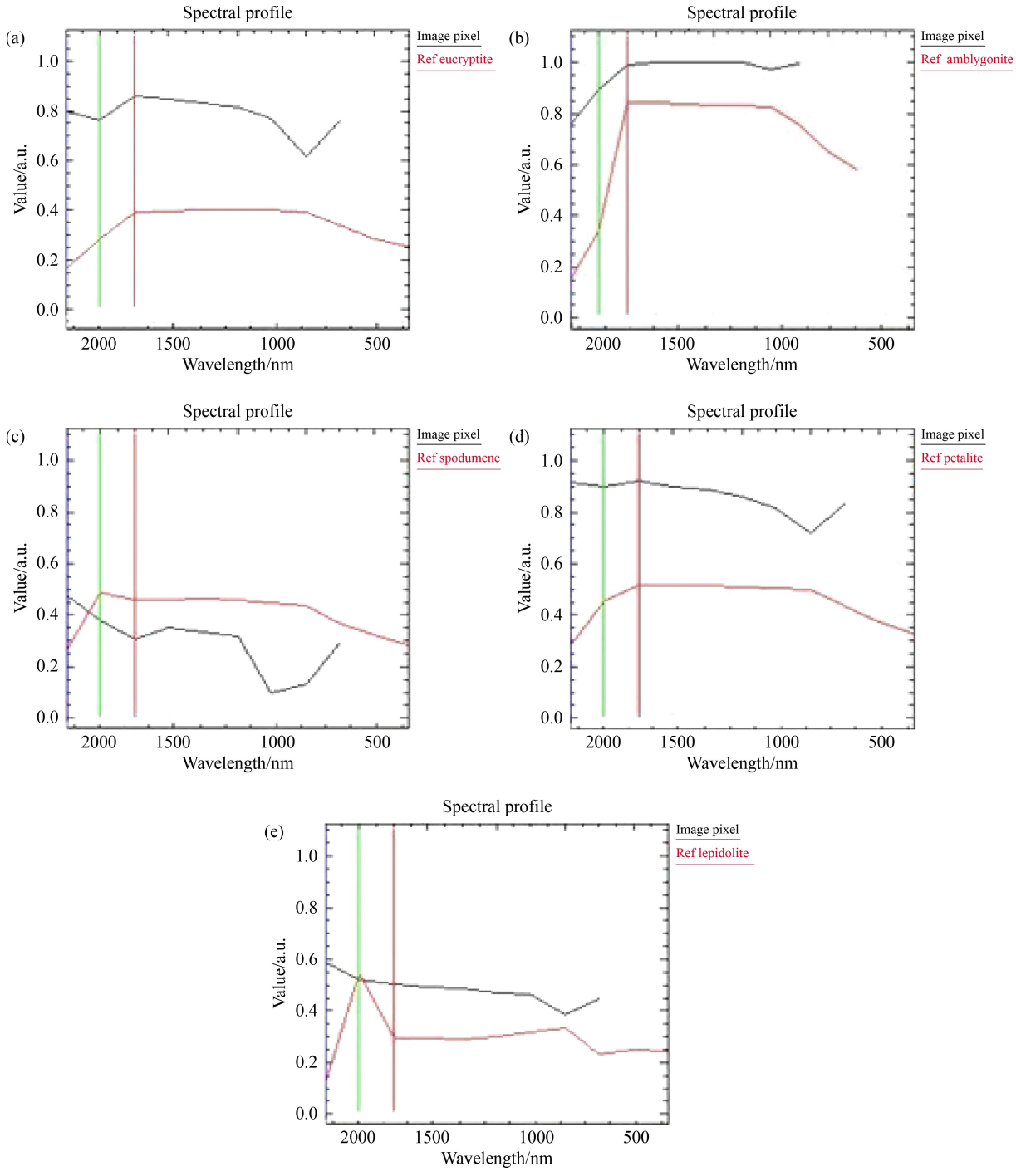

Fig. 15 The similarity matching of (a) eucryptite, (b) amblygonite, (c) spodumene, (d) petalite, and (e) lepidolite.

RGBs can only map LCMs without distinguishing their type. Therefore, in the next step, three band ratios mentioned in Cardoso-Fernandes et al. (2019a, 2019b) were applied for distinguishing amblygonite, lepidolite, and spodumene (Fig. 17).

In evaluating the results of applying the above band ratios for distinguishing LCMs, a comparison between spectral curves of the lithium minerals identified in the above maps and spectral curves of the reference LCMs was performed (Fig. 18).

As can be seen above, in Fig. 18(a) middle part of the spectral curve of the amblygonite identified using a 12/9 ASTER band ratio is more similar to the spectral curve of the reference spodumene. The spectral curve of the identified spodumene (Fig. 18(b)) and lepidolite (Fig. 18(c))(based on 1/3 and 6/2 ASTER band ratios, respectively) are mostly similar to the reference petalite in the middle part. It can be concluded that these band

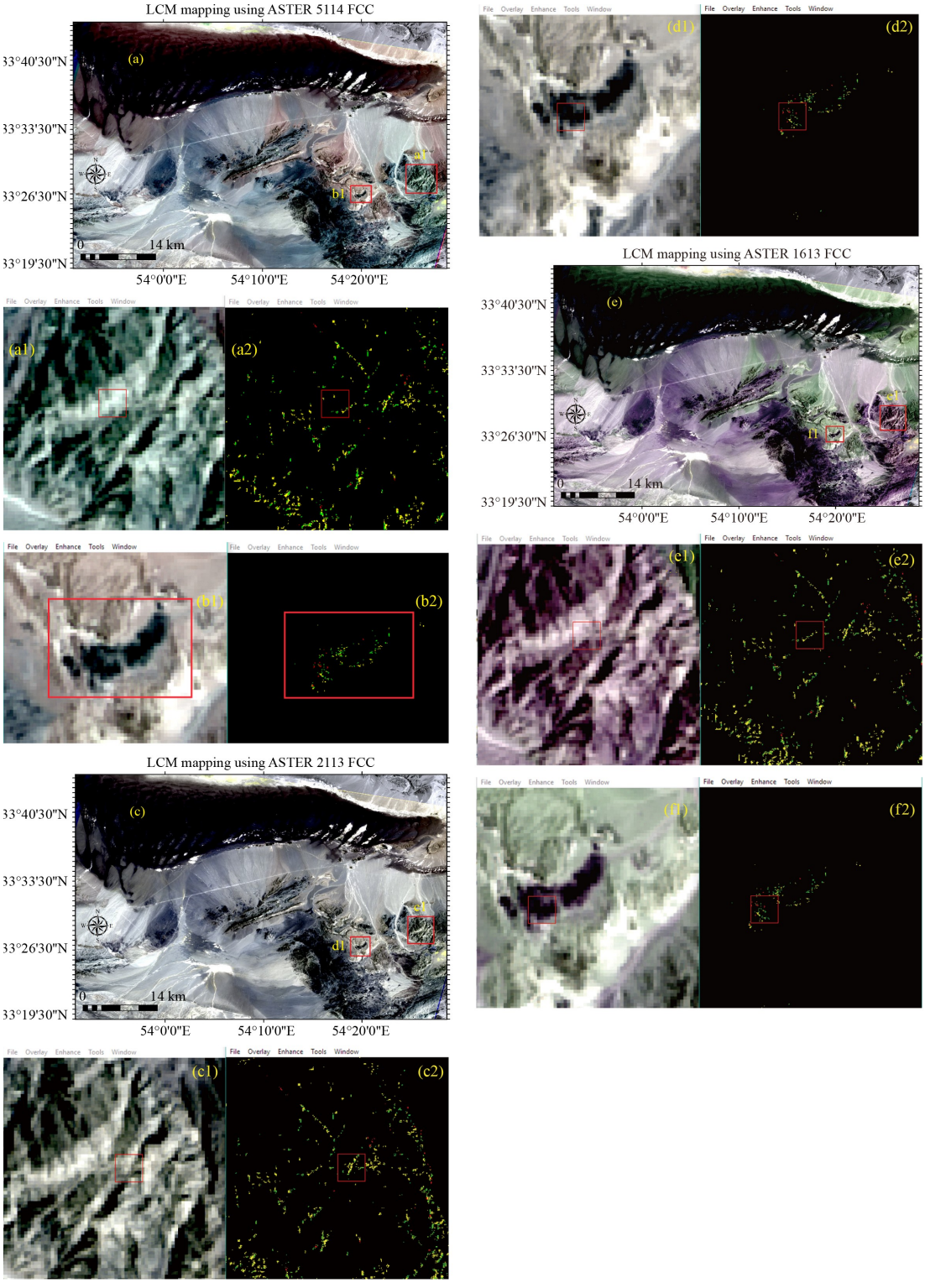

Fig. 16 LCM mapping using ASTER image: (a) 5114 RGB, (a1, b1) zoomed parts of LCM mapping based on 5114 RGB, (a2, b2) SAM outputs using S2A image, (c) 2113 RGB, (c1, d1) zoomed parts of LCM mapping based on 2113RGB,(c2, d2) SAM outputs using S2A image, (e) 1613 RGB, (e1, f1) zoomed parts of LCM mapping based on 1613RGB, (e2, f2) SAM outputs using S2A image.

ratios and also the RGBs are very beneficial for Li containing regions identification but not for distinguishing different LCMs types.

6 Conclusions

The main purpose of the present study was to investigate

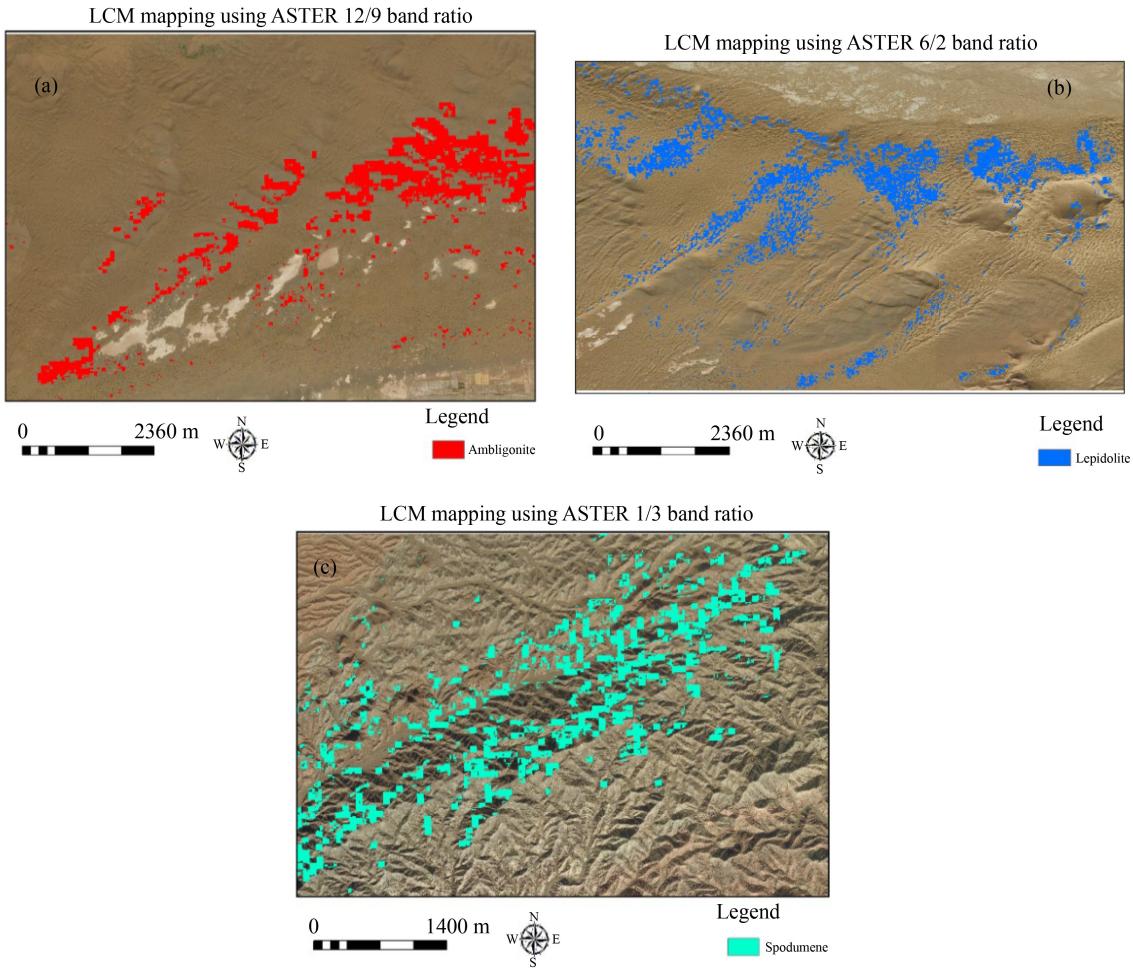

Fig. 17 LCM mapping: (a) amblygonite mapping using 12/9 ASTER band ratio, (b) lepidolite mapping using 6/2 ASTER band ratio, and (c) spodumene mapping using 1/3 ASTER band ratio.

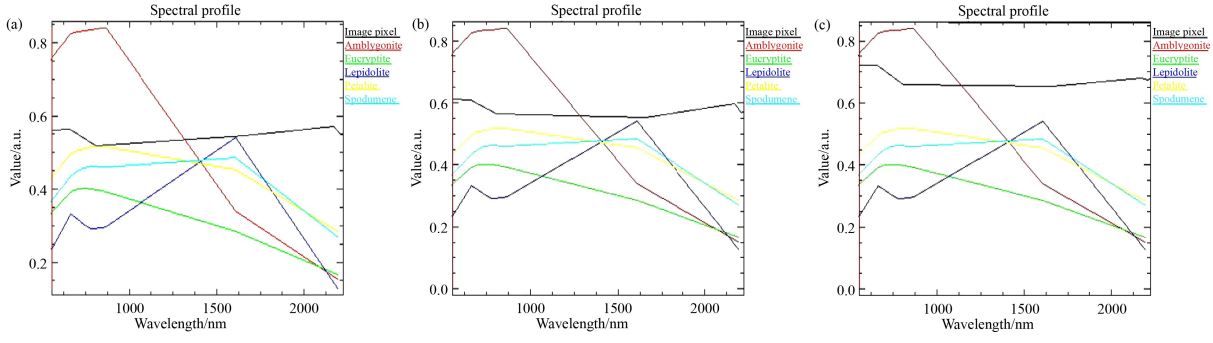

Fig. 18 The similarity matching of (a) amblygonite, (b) spodumene, and (c) lepidolite.

the capability of Sentinel-2 image and FieldSpec3 for LCMs mapping of a part of central Iran. Another purpose of this study was to compare the spectral characteristics of five important LCMs, including spodumene, lepidolite, amblygonite, petalite, and eucryptite accurately. Therefore, after creating the spectral curves of the LCMs using FieldSpec3, the spectral curves underwent rigorous analyses using the TSG and the Prism software. It was found that each mineral absorption feature has different properties such as position, depths, FWHM, etc. Therefore, minerals can be easily discriminated by studying their spectral characteristics.

An important absorption feature of LCMs was the lithium absorption center, which showed minor differences and can be used to discriminate and identify these minerals. The lithium absorption center has a noticeable shift, different depth, and FWHM in the LCMs. Since lepidolite and eucryptite have the highest and the lowest lithium absorption depth, respectively,

therefore it can be concluded that lepidolite has the highest and eucryptite has the lowest amount of lithium in comparison with other studied LCMs. Other absorbing elements such as OH^-, H_2O, etc., showed differences in the LCMs as well.

For mapping LCMs in the study area, after confirming the LCMs in several samples of pegmatite rocks of the Central Iranian Terrane (using field survey and spectrographic analyses performed by other researchers), the SAM classifier has been used. The classification results showed the presence of spodumene, amblygonite, petalite, and eucryptitein several places in the study area. An accurate comparison of the classified minerals spectral curves based on the SAM with the reference LCMs showed suitable matches. The results indicated that spectroscopy and the SAM classification of Sentinel-2 image have high capability to identify, discriminate and map rare minerals such as LCMs. Applying the SID classifier obtained poor results for LCM mapping. LCM mapping was also done using different RGBs and band ratios of the ASTER image. The results showed that these band ratios and also the RGBs are very beneficial for Li containing regions identification but not for distinguishing different LCMs types.

Acknowledgments This study was supported by university grant (No. 97.3.02.26247), for which the authors are thankful to the Shahid Chamran University of Ahvaz-Iran. The authors are also grateful to the ESA for providing the required satellite data.

References

Afsharifar S, Rangzan K (2014). Evaluation of spectral absorption depth of Zagros Dolomite using FieldSpec3, SAMS and Prism software. In: 32 international Congress of Earth Sciences (in Persian)

Alamdar K, Kuhsari A H, Ansari A (2008). A preliminary study on the potential of Lithium on Iran's pegmatite rocks. In: 16th Iranian Conference of Crystallography and Mineralogy (in Persian)

Amidi SM, Michel R (1985). Cenozoic magmatism of the Surk area (Central Iranian terrane) stratigraphy, petrography, geochemistry, and their geodynamic implications. Geology Alpine: 61

Berberian M, King G C P (1981). Towards a paleogeography and tectonic evolution of Iran. Can J Earth Sci, 18(2): 210–265

Birch N J, Robinson D, Inie R A, Hullin R P (1978). Lithium-6 stable isotope determination by atomic absorption spectroscopy and its application to pharmacokinetic studies in man. J Pharm Pharmacol, 30(1): 683–685

Cardoso-Fernandes J, Teodoro A C, Lima A (2019a). Remote sensing data in lithium (Li) exploration: a new approach for the detection of Li-bearing pegmatites. Int J Appl Earth Obs Geoinf, 76: 10–25

Cardoso-Fernandes J, Lima A, Roda-Robles E, Teodoro A C (2019b). Constraints and potentials of remote sensing data/techniques applied to lithium (Li)-pegmatites. Can Mineral, 57(5): 723–725

Cardoso-Fernandes J, Teodoro A C, Lima A, Perrotta M, Roda-Robles E (2020). Detecting lithium (Li) mineralizations from space: current research and future perspectives. Appl Sci (Basel), 10(5): 1785

Cardoso-Fernandes J, Silva J, Dias F, Lima A, Teodoro A C, Barrès O, Cauzid J, Perrotta M, Roda-Robles E, Ribeiro M A (2021). Tools for remote exploration: a lithium (Li) dedicated spectral library of the Fregeneda–Almendra Aplite–Pegmatite field. Data, 6(3): 33–43

Cao M, Qin K, Li G, Evans N J, Hollings P, Maisch M, Kappler A (2017). Mineralogical evidence for crystallization conditions and petrogenesis of ilmenite-series I-type granitoids at the Baogutu reduced porphyry Cu deposit (western Junggar, NW China): Mössbauer spectroscopy, EPM and LA-(MC)-ICPMS analyses. Ore Geo Rev, 86: 382–403

Clark R N (1999). Spectroscopy of rocks and minerals, and principles of spectroscopy. Man Remot Sens, 3: 3–58

Cloutis E A, Klima R L, Kaletzke L, Coradini A, Golubeva L F, McFadden L A, Shestopalov D I, Vilas F (2010). The 506 nm absorption feature in pyroxene spectra: nature and implications for spectroscopy-based studies of pyroxene-bearing targets. Icarus, 207(1): 295–313

Delaloye M, Jenny J, Stampfli G (1981). K-Ar dating in the eastern Elburz (Iran). Tectonophysics, 79(1−2): T27–T36

Derakhshi M, Ghasemi H, Sahami T (2014). Geology and petrology of the SoltanMaydan basaltic complex in north–northeast of Shahrudm Eastern Alborz, North of Iran. Geoscience, 23: 63–76

Du Y, Chang C, Ren H, Chang C, Jensen J O, D'Amico F (2004). New hyperspectral discrimination measure for spectral characterization. Opt Eng, 43(8): 1777–1786

Gao Y, Bagas L, Li K, Jin M, Liu Y, Teng J (2020). Newly discovered Triassic lithium deposits in the Dahongliutan area, northwest China: a case study for the detection of lithium-bearing pegmatite deposits in rugged terrains using remote-sensing data and images. Front Earth Sci, 8: 591966

Ghorbani M (2016). Economic Geology of Iran, Mineral Deposits and Natural Resources Springer. Geol: 569

Guha A, Kumar K V, Porwal A, Rani K, Sahoo K C, Kumar S A, Diwakar P G (2018). Reflectance spectroscopy and ASTER based mapping of rock-phosphate in parts of Paleoproterozoic sequences of Aravalli group of rocks, Rajasthan, India. Ore Geol Rev, 108: 83–87

Kendall T G (2017). An investigation of infrared spectral features related to the presence of lithium in micas, east Kemptville tin deposit, Nova Scotia. Dissertation for the Bachelor's Degree. Halifax: Saint Mary's University

Kuching S (2007). The performance of maximum likelihood, spectral angle mapper, neural network and decision tree classifiers in hyperspectral image analysis. J Computer Sci, 3(6): 419–423

Kruse F A (2010). Mineral mapping using spectroscopy: from field measurements to airborne and satellite-based imaging spectrometry. In: Proc ASARS Symp

Liu D, Han L (2017). Spectral curve shape matching using derivatives in hyperspectral images. IEEE Geosci Remote Sens Lett, 14(4): 504–508

Meshram P, Pandey B D, Mankhand T R (2014). Extraction of Lithium from primary and secondary sources by pre-treatment, leaching, and separation: a comprehensive review. Hydrometallurgy, 150: 192–208

Noda S, Yamaguchi Y (2017). Estimation of surface iron oxide

abundance with suppression of grain size and topography effects. Ore Geo Rev, 83: 312–320

Pohl C, Van Genderen J L (2016). Remote Sensing Image Fusion: A Practical Guide. Boca Raton: CRC Press

Rangzan K, Kabolizadeh M, Karimi D, Saberi A (2019). Applied Mineral Spectroscopy. Ahvaz: Shahid Chamran University of Ahvaz (in Persian)

Rangzan K, Beyranvand S, Pourkaseb H, Ranjbar H, Zarasvandi A (2020). Applying spectral analysis for identification of alteration zones in north Saveh area. Iran J Spectral Imag: 9

Rossi C, Spittle S, Bayaraa M, Pandey A, Henry N (2018). An earth observation framework for the lithium exploration. In: IGARSS 2018–2018 IEEE International Geoscience and Remote Sensing Symposium: 1616–1619

Rahmati I M (2010). Metamorphism and geotectonic position of the ShoturKuh Complex, Central Iranian Block. Dissertation for the Doctoral Degree. Prague: Charles University

Shah H E, Ashja Ardalan A, Emami M H, Razavi M H (2014). The petrology and geochemistry of granitoid rocks of Troud area in southwest of Shahrood. Iranian J Earth Sci, 6: 64–77

Soltani A (2000). Geochemistry and geochronology of I-type granitoid rocks in northeastern of Central Iranian terraneplace. Dissertation for the Doctoral Degree. Wollongong: University of Wollongong

Stocklin J (1968). Structural history and tectonics of Iran: a review. AAPG Bull, 52(7): 1229–1258

Tappert M C, Rivard B, Giles D, Tappert R, Mauger A (2013). The mineral chemistry, near-infrared, and mid-infrared reflectance spectroscopy of phengite from the Olympic Dam IOCG deposit, South Australia. Ore Geo Rev, 53: 26–38

Zaini N (2009). Calcite-Dolomite mapping to assess dolomitization patterns using laboratory spectra and hyperspectral remote sensing. Dissertation for the Master's Degree. Southampton: University of Southampton (UK)

Zheng G, Jiao C, Zhou S, Shang G (2016). Analysis of soil chronosequence studies using reflectance spectroscopy. Int J Remote Sens, 37(8): 1881–1901